Magnetization dynamics due to field interplay in external field free spin Hall nano-oscillators

Ayush K. Gupta,[1] Sourabh Manna,[2] Rajdeep Singh Rawat,[2] and Rohit Medwal[1,*]
[1]*Department of Physics, Indian Institute of Technology Kanpur, Kanpur 208016, India*
[2]*Natural Sciences and Science Education, National Institute of Education, Nanyang Technological University, Singapore 637616*

(Received 19 August 2023; revised 6 March 2024; accepted 7 March 2024; published 15 April 2024)

Spin Hall nano-oscillators (SHNOs) have shown applications in unconventional computing schemes and broadband frequency generation in the presence of applied external magnetic field. However, under external magnetic field free conditions, the oscillation characteristics of nanoconstriction-based SHNOs exhibits a notable reliance on the effective field, which can be adjusted by varying the constriction width. In this study, we explore how the width of the nanoconstriction affects the magnetization dynamics in field free SHNOs assisted by anisotropy. In uniaxial anisotropy-based field free SHNOs, either the anisotropy field (B_{anis}) or the demagnetization field (B_{demag}) dominates the magnetization dynamics depending on the constriction width. Our findings reveal distinct auto-oscillation characteristics in narrower constrictions with 20- and 30-nm constriction width compared to their wider counterpart with 100-nm width. The observed frequency shift variations with input current (I_{dc}) and constriction widths stem from the inherent nonlinearity of the system. The interplay between the B_{demag} and B_{anis}, controlled by constriction width, yields rich dynamics, and offers control over frequency and amplitude of auto-oscillations, and the threshold current needed for auto-oscillations. Notably, the spatial configuration of spin-wave wells within the constriction undergoes transformations in response to changes in both constriction width and anisotropy. The findings highlight the significant influence of competing internal fields at the constriction on the field free auto-oscillations of SHNOs, with the impact intensifying as the constriction width is varied.

DOI: 10.1103/PhysRevB.109.134421

I. INTRODUCTION

The growing reliance on technological devices in our daily lives has led to a quest for faster and more efficient computing and memory devices [1]. Recently, spin Hall nano-oscillator (SHNO) devices have garnered attention due to their simple fabrication process [2], scalability [3], and reduced Joule heating. Moreover, SHNOs showcase remarkable characteristics such as high-frequency tunability [4,5] and synchronization to external microwave and mutual synchronization [6–10], highlighting their potential in broadband frequency generation [5] and various neuromorphic computing schemes [1,11]. Markovic *et al.* have demonstrated that SHNOs can emulate voltage spikes akin to biological neurons [12]. Additionally, SHNOs' nonlinear traits can be adjusted through gate-voltage modulation [13–15]. Exploiting the inherent nonlinear magnetization dynamics in SHNOs, a wide array of spin-wave modes can be excited, including propagating spin waves (SWs) [16–18], droplet solitons [19,20], and localized bullet modes [2,21]. Chen *et al.* [22] have illustrated a method to leverage the nonlinear coupling among these diverse modes. Furthermore, skyrmion-like topological states can be generated in the oscillating region of the device, offering potential applications in topologically stable spin-torque devices [23]. The nonlinear characteristics of SHNOs can be finely tuned via input dc current and applied gate voltage [13–15], making them promising candidates for magnonic (spin-wave) devices in information processing [16,24,25].

SHNO devices utilize the spin Hall effect (SHE) [26], a phenomenon which leads to the conversion of charge current into pure spin current [27] in a material with high spin-orbit coupling, such as heavy metals. A typical SHNO device comprises a ferromagnetic layer interfaced with a heavy-metal layer. The spin current generated in the heavy-metal layer through SHE diffuses into the adjacent ferromagnetic layer, inducing a dampinglike spin-orbit torque on the magnetization [28]. Adequate spin-orbit torque damping counteracts intrinsic damping, facilitating sustained magnetization oscillations around $\boldsymbol{B}_{\text{int}}$.

Although typically a biasing dc magnetic field is necessary for SHNO operation [29], recent studies demonstrate that a biasing field is not essential for sustained auto-oscillation [30–32]. Bias field free SHNOs offer benefits such as lower energy consumption, enhanced scalability, and improved compatibility for complementary metal-oxide semiconductor integration. The field free SHNOs pave the way for a multitude of power-efficient applications such as mimicking the neural synapses, unconventional computing schemes [10], and low-cost training of neural networks [11]. In the case of uniaxial anisotropy-assisted field free SHNOs, magnetization dynamics is influenced by the corresponding anisotropy field and the demagnetization field. However, the interplay between these fields and their impact on SHNO magnetization dynamics remains poorly understood. In nanoconstriction (NC) SHNO, modulation of the demagnetization field with the

*rmedwal@iitk.ac.in

constriction width significantly affects the frequency, precession amplitude, linewidth, and threshold current needed to initiate the auto-oscillations. This makes it a crucial geometrical parameter for optimizing SHNO device miniaturization.

In the present study, we systemically investigate the influence of constriction width on the auto-oscillation characteristics of a bias field free NC SHNO. Bias field free auto-oscillations are achieved by introducing a uniaxial anisotropy in the ferromagnetic layer, where $\boldsymbol{B}_{\text{int}}$ comprises anisotropy field ($\boldsymbol{B}_{\text{anis}}$), demagnetization field ($\boldsymbol{B}_{\text{demag}}$) due to dipolar interactions, and the current-induced Oersted field ($\boldsymbol{B}_{\text{Oe}}$). Notably, the $\boldsymbol{B}_{\text{demag}}$ is highly dependent on the constriction width. For smaller constriction width, the edges are closer to each other, resulting in an increase in dipolar interaction energy as well as $\boldsymbol{B}_{\text{demag}}$. Conversely, $\boldsymbol{B}_{\text{anis}}$ remains unaffected by constriction width and instead depends on the magnetocrystalline anisotropy in the system. Consequently, wider ($\boldsymbol{B}_{\text{anis}} > \boldsymbol{B}_{\text{demag}}$) and narrower ($\boldsymbol{B}_{\text{anis}} < \boldsymbol{B}_{\text{demag}}$) constrictions exhibit distinct dominant components in the total internal field $\boldsymbol{B}_{\text{int}}$ at the constriction region, affecting auto-oscillation frequency variation with current for different constriction widths. The change in auto-oscillation frequency of SHNOs with different constriction widths is determined by the interplay between the anisotropy field and the demagnetization field. Additionally, we discuss how the nonlinearity coefficient N, representing the nonlinear behavior of auto-oscillation frequency, changes sign with decreasing constriction width. Finally, we examine substantial differences in the spatial profile of auto-oscillation modes with varying constriction width.

II. METHODOLOGY

The magnetization dynamics of a ferromagnet is governed by two major torques: a precessional torque due to the effective magnetic field and a damping torque resulting from electron-phonon and electron-impurities scattering within the material. The magnetization dynamics can be expressed by the Landau-Lifshitz-Gilbert (LLG) equation, given as

$$\frac{\partial \boldsymbol{M}}{\partial t} = (-\gamma \boldsymbol{M} \times \boldsymbol{B}_{\text{int}}) + \left(\frac{\alpha}{M_s}\boldsymbol{M} \times \frac{\partial \boldsymbol{M}}{\partial t}\right). \tag{1}$$

Here, the first term is the precessional torque τ_p acting on the magnetization M, which is tangential to the precession trajectory, and the second term is the damping torque τ_D pointing towards $\boldsymbol{B}_{\text{int}}$. To maintain sustained precession of magnetization around $\boldsymbol{B}_{\text{int}}$, an opposing torque τ_{AD} must counteract the damping. This additional antidamping (AD) torque can be produced through the injection of spin current into the ferromagnetic (FM). The high spin-orbit coupling in the heavy metal (HM) layer facilitates the conversion of the applied charge current into a transverse spin current denoted by $\boldsymbol{J_s} = (\frac{I_{\text{dc}}}{I_{\text{ref}}})\theta_{\text{SH}}|J_c|$ [19]. Here, θ_{SH} is the spin Hall angle of HM and $|J_c|$ is the current density at I_{ref}. The injected $\boldsymbol{J_s}$ gives rise to the antidamping torque $\boldsymbol{\tau}_{\text{AD}}$ that acts opposite to the damping torque and tries to orient the $\boldsymbol{M}$ along the spin-polarization direction $\boldsymbol{\sigma}$. The $\boldsymbol{\tau}_{\text{AD}}$ is typically of Slonczewski form, which is given by Eq. (2) [33]:

$$\boldsymbol{\tau}_{\text{AD}} = \frac{|J_c|\hbar\theta_{\text{SH}}}{2et_{\text{FM}}\mu_o M_s}(\boldsymbol{M} \times (\boldsymbol{\sigma} \times \boldsymbol{M})). \tag{2}$$

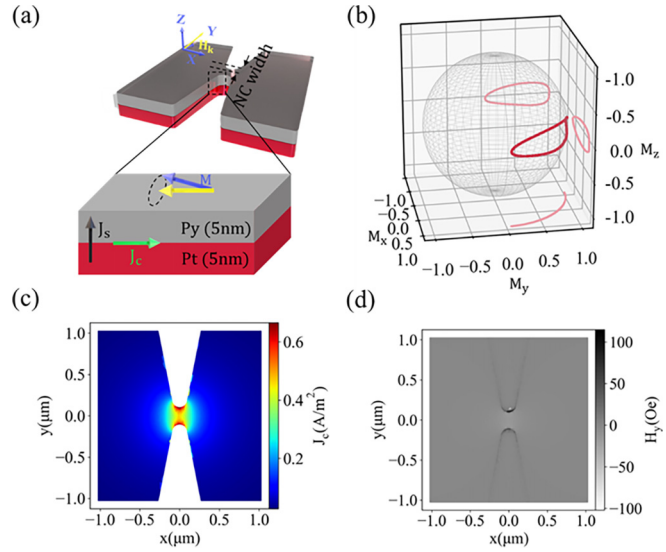

FIG. 1. (a) System schematic shows the SHNO and directions of spin current, charge current, and $\boldsymbol{B}_{\text{anis}}$. (b) Trajectory traced by the head of magnetization for 100-nm constriction for $K_u = 10\frac{\text{kJ}}{\text{m}^3}$ at I_{th} along with projections. (c) Spatial profile of current density for 100-nm constriction width. (d) Spatial profile of y component of Oersted field for 100-nm constriction width.

Here, t_{FM} is the thickness of the FM layer. The fieldlike torque τ_{FL} due to J_s is disregarded due to its relatively low magnitude compared to $\boldsymbol{\tau}_{\text{AD}}$ [34]. Therefore, magnetization dynamics can be described using the Landau-Lifshitz-Gilbert-Slonczewski equation [28,35]:

$$\frac{\partial \boldsymbol{M}}{\partial t} = (-\gamma \boldsymbol{M} \times \boldsymbol{H}_{\text{eff}}) + \left(\frac{\alpha}{M_s}\boldsymbol{M} \times \frac{\partial \boldsymbol{M}}{\partial t}\right) + \frac{|J_c|\hbar\theta_{\text{SH}}}{2et_{\text{FM}}\mu_o M_s}(\boldsymbol{M} \times (\boldsymbol{\sigma} \times \boldsymbol{M})). \tag{3}$$

NC width-dependent field free auto-oscillations are examined by designing the SHNO as a Py (5 nm)/Pt (5 nm) bilayer stack with NC geometry and varying constriction widths. The stack, measuring 5 μm × 5 μm, incorporates a round NC at the center, characterized by an opening angle of 22 ° and a radius of curvature of 50 nm. Using COMSOL®, this geometry is simulated in air, with an electric current applied to the YZ face [Fig. 1(a)] along the x direction. The current-density distribution and the associated Oersted field profile at the reference current $I_{\text{ref}} = 1$ mA [Figs. 1(b) and 1(c)] are obtained from COMSOL® simulations. Given the relatively lower conductivity of the Py layer (3.12×10^6 S/m) compared to the Pt layer (8.9×10^6 S/m), the majority (74%) of the current flows through the Pt layer, rendering the spin filtering effect negligible in the FM layer. The spin Hall effect in the Pt layer generates a pure spin current with $-y$ polarization that diffuses into the Py layer, perpendicular to the XY plane. The Py layer is discretized into a grid of $512 \times 512 \times 1$ rectangular cells, with each cell measuring $2 \times 2 \times 5\,\text{nm}^3$, which is smaller than the Py's exchange length along the lateral directions. The material parameters of Py are defined as follows: gyromagnetic ratio $\gamma = 29.53$ GHz/T, damping constant $\alpha = 0.02$, saturation magnetization $M_s = 8 \times 10^5$ A/m,

TABLE I. Easy-axis angle and maximum value of J_c at constriction for different constriction widths.

NC width (nm)	J_c $\left(\frac{\text{TA}}{\text{m}^2}\right)$	ϕ (deg)
20	2.727	90
30	1.818	90
40	1.407	80
60	1.006	80
80	0.797	70
100	0.665	70

and exchange constant $A_{ex} = 12 \times 10^{-12}$ J/m [8]. The magnetization dynamics is obtained by numerically integrating the LLG equation. Initially, the magnetization is relaxed for 5 ns before applying I_{dc}. The magnetization dynamics is simulated for a total of 45 ns for each I_{dc} value, excluding the initial 15 ns to account for stable precession and eliminate transient effects. Frequency of the auto-oscillations f is extracted by performing fast Fourier transform (FFT) over the stable regime of oscillations.

To avoid the need for an external biasing field, we leverage the inherent uniaxial anisotropy of the ferromagnetic material. We explore the oscillation properties of such a bias free SHNO under the influence of an anisotropy field. Simulations were conducted by varying the dc current, uniaxial anisotropy constant (K_u), and the easy-axis orientation. Easy-axis angle is defined such that it maximizes the amplitude of auto-oscillations. The easy axis approaches the y axis for narrower constrictions, while increasing the constriction width causes the easy axis to shift towards the x axis [see Appendix C (Fig. 8)]. This behavior arises from the dipolar interaction originated from the geometrical confinement at the constriction region, characterized by the constriction width. (See Table I.)

III. RESULTS

The width-dependent field free auto-oscillations are studied for NC width ranging from 100 to 20 nm, and uniaxial anisotropy values varying from $K_u = 5$ to 15 kJ/m^3. Figure 1(b) depicts the magnetization trajectory during auto-oscillations for a 100-nm NC width at $K_u = 10$ kJ/m^3. It was observed that regardless of the anisotropy values, the dynamics for the 100-nm width shows a decrease in frequency with an increase in current. Increment in the anisotropy (K_u) leads to an increase in auto-oscillation amplitude due to the closer proximity of spin-wave wells. This is attributed to the increase value of $\boldsymbol{B}_{\text{int}}$. The decrease in frequency with input current was observed from the constriction width of 100 to 40 nm [see Appendix E and Fig. 2(a)]. In contrast, the 30-nm constriction initially shows a frequency increase with minimal tunability at high I_{dc} [Fig. 2(b)], whereas the 20-nm constriction does not exhibit a linear trend of frequency with current [see Fig. (2c)].

The change in the total internal magnetic field $\boldsymbol{B}_{\text{int}}$ at the constriction leads to the different trends of the current-driven tunability of auto-oscillation frequency . In our case, $\boldsymbol{B}_{\text{int}}$ also has an additional contribution from $\boldsymbol{B}_{\text{anis}}$ along with $\boldsymbol{B}_{\text{Oe}}$, and $\boldsymbol{B}_{\text{demag}}$ due to the uniaxial anisotropy present in the system. The anisotropy field $\boldsymbol{B}_{\text{anis}}$ is represented by

$$\boldsymbol{B}_{\text{anis}} = \frac{2K_u}{M_s} \cos\,\theta \hat{\boldsymbol{u}}. \tag{4}$$

The $\hat{\boldsymbol{u}}$ is the direction of the easy axis and θ is the angle between magnetization M and $\hat{\boldsymbol{u}}$. The $|\boldsymbol{B}_{\text{anis}}|$ decreases as the amplitude of the oscillations is increased. This occurs because the dampinglike torque is proportional to charge current, $\boldsymbol{\tau}_{\text{AD}} \propto J_c$ [28]. Consequently, the precession cone angle (θ) increases with charge current, leading to a reduction in cos θ as well as $|\boldsymbol{B}_{\text{anis}}|$. The magnitude of $\boldsymbol{B}_{\text{demag}}$ is also influenced by the amplitude of auto-oscillation. Specifically, the component of $\boldsymbol{B}_{\text{demag}}$ along a direction scales proportionately with the magnitude of magnetization in that direction. Higher auto-oscillation amplitudes decrease the magnetization along the easy axis, leading to a reduced contribution from B_{demag}. The y component of $\boldsymbol{B}_{\text{int}}$, taking $\boldsymbol{B}_{\text{anis}}$ and $\boldsymbol{B}_{\text{demag}}$ into account, can be written as

$$\boldsymbol{B}^y_{\text{int}} = \frac{2K_u}{M_s} \cos\,\theta m_y \hat{\boldsymbol{y}} + \boldsymbol{B}^y_{\text{demag}} + \boldsymbol{B}^y_{\text{Oe}}. \tag{5}$$

Figure 3 illustrates the current dependence of the y component of $\boldsymbol{B}_{\text{anis}}$, $\boldsymbol{B}_{\text{int}}$, and $\boldsymbol{B}_{\text{demag}}$ at $K_u = 10$ kJ/m^3 across various constriction widths. Values of different fields at the center of the constriction were obtained by defining a very small region ($20 \times 20 \times 5$ nm^3) at the center. B_{anis}, B_{demag}, and B_{int} shown in Fig. 3 are the time-averaged values over the stable regime of the oscillation and the area of the defined small region. Across all three constrictions, a decrease

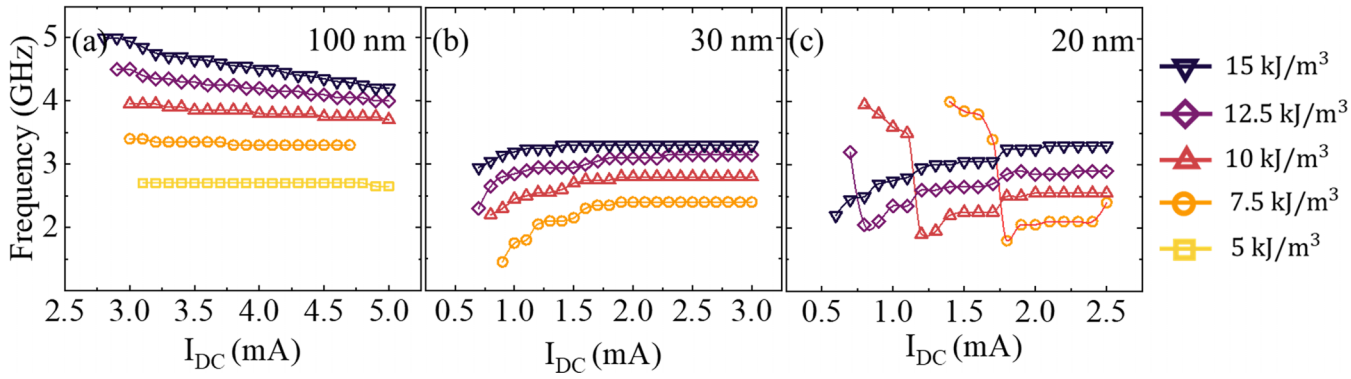

FIG. 2. Variation of the frequency of auto-oscillations with input current for different constriction sizes at different K_u values.

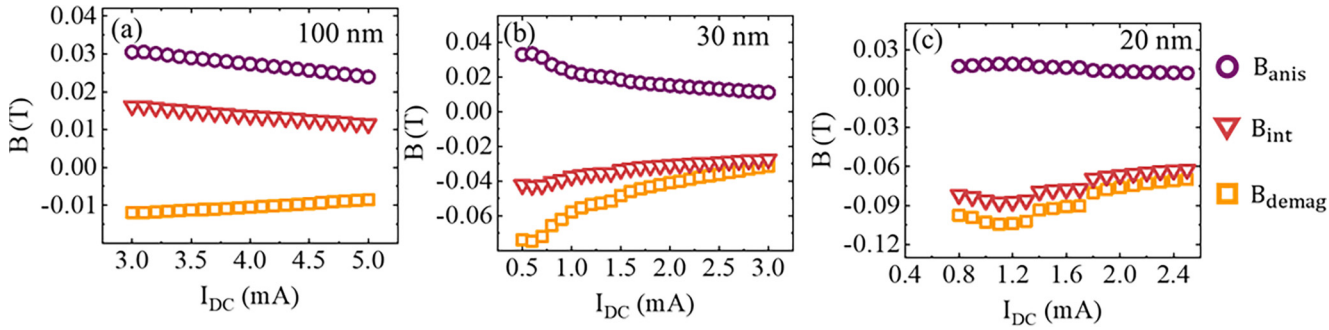

FIG. 3. Variation of the y component of $\boldsymbol{B}_{\text{anis}}$, $\boldsymbol{B}_{\text{demag}}$, and $\boldsymbol{B}_{\text{int}}$ at the center of constriction with input current for different constriction width at $K_u = 10\ \text{kJ/m}^3$.

in both $\boldsymbol{B}_{\text{anis}}$ and $\boldsymbol{B}_{\text{demag}}$ is noted with increasing input dc current. This decrease is attributed to the increased oscillation amplitude resulting from the increased current, as discussed in the preceding paragraph. It is also interesting to see that for the smallest NC width of 20 nm, $\boldsymbol{B}_{\text{demag}}$ is approximately ten times larger than that of the 100 nm. This disparity is due to the inverse relationship between the dipolar interaction energy at the constriction center and the constriction width.

The primary contribution to $\boldsymbol{B}_{\text{int}}$ for 20-nm NC stems from the $\boldsymbol{B}_{\text{demag}}$ [Fig. 3(c)], whereas for 100-nm constriction the predominant contribution comes from $\boldsymbol{B}_{\text{anis}}$ [Fig. 3(a)]. Consequently, the $\boldsymbol{B}_{\text{int}}$ for small NC width follows $\boldsymbol{B}_{\text{demag}}$ instead of $\boldsymbol{B}_{\text{anis}}$, contrary to the behavior observed in large constriction widths (see Appendix A, Fig. 6).

The behavior of B_{int} dictates the magnetodynamic nonlinearity of the SHNO. B_{int} varies significantly with constriction width and as a function of input current. As a result, the magnetodynamic characteristics of field free SHNOs differ significantly across the three constriction widths. To gain a deeper insight, we apply the theory of spin torque-induced nonlinear auto-oscillation in a thin-film ferromagnet subjected to an in-plane biasing magnetic field. This theory describes the rate of change of the complex spin-wave amplitude $(\frac{\delta b}{\delta t})$ as given by Eq. (6) [21]:

$$\frac{\delta b}{\delta t} = -i[\omega_o - D\Delta b + N|b|^2 b] - \Gamma b + f\left(\frac{r}{R_c}\right)\sigma I b - f\left(\frac{r}{R_c}\right)\sigma I|b|^2 b. \tag{6}$$

Here, ω_o represents the ferromagnetic resonance (FMR) frequency, $D = \frac{2A_{ex}}{M_s}\frac{\delta\omega_o}{\delta H}$ is spin-wave dispersion coefficient, R_c is related to the effective area of spin current injection, $\Gamma = \alpha(\omega_H + \frac{\omega_M}{2})$ is spin-wave dissipation rate with $\omega_H = \gamma H_{\text{int}}$, $\omega_M = 4\pi\gamma M_s$. N is the nonlinear frequency shift given by

$$N = -\frac{\omega_H \omega_M\left(\omega_H + \frac{\omega_M}{4}\right)}{\omega_o\left(\omega_H + \frac{\omega_M}{2}\right)}. \tag{7}$$

Consider a localized nonpropagating spin-wave mode, $b = B_o\psi(\frac{r}{l})e^{-i\omega t}$, where ψ describes the spatial profile of the oscillation mode. The frequency of the oscillations is given as $\omega = \omega_o + NP$, where $P = |B_o|^2$ is the power of the oscillations, which can be derived from the amplitude of auto-oscillation, and ω_o is the FMR frequency. We have calculated this FMR frequency by using Kittel's formula. The $\boldsymbol{B}_{\text{int}}$ value corresponding to the driving current is used to calculate the FMR frequency as a function of driving current. Thin-film approximation has been used to estimate the value of the FMR frequency for the 100-nm constriction.

The value of N depends on the $\boldsymbol{B}_{\text{int}}$ and differs across all three constrictions. For SHNOs with in-plane fields the value of N can be approximated with Eq. (7) (see Appendix D). It can be deduced from Eq. (7) that for positive $\boldsymbol{B}_{\text{int}}$, the nonlinear frequency shift will be negative. This is evident in the 100-nm constriction [Fig. 3(a)], where $\boldsymbol{B}_{\text{int}}$ is dominated by $\boldsymbol{B}_{\text{anis}}$ and remains positive [see Appendix A (Fig. 6)] for all K_u values throughout the I_{dc} sweep. Consequently, the auto-oscillation frequency exhibits a redshift as a function of current for 100-nm constriction. In contrast, N is positive for 30-nm constriction at lower values of I_{dc}. However, at higher I_{dc}, N is almost constant because of minuscule change in $\boldsymbol{B}_{\text{int}}$. As a result, the frequency behavior shows a blueshift for low I_{dc}; for high I_{dc} frequency is constant with current [Fig. 2(b)]. The frequency response of the 20-nm constriction exhibits a near-consistent blueshift across all current values, attributed to the positive nonlinear frequency shift [Fig. 2(c)]. The abrupt drop in frequency for some anisotropy values is observed for 20 nm. The is because at the point of frequency drop the trajectory of the oscillations widens. The power of oscillation is suddenly increased when the trajectory of the oscillations becomes wider. These lead to the sudden decrease in the frequency as the frequency of auto-oscillation as per $\omega = \omega_o + NP$ is related to both the magnetodynamic nonlinearity N and the power of oscillation P. We further note that an increase in K_u results in higher value of B_{anis} and B_{int}. Therefore, the auto-oscillation frequency generally rises with higher K_u, regardless of constriction widths. This control over the nonlinearity coefficient may be useful to selectively excite the different dynamical modes of oscillations [36].

In addition to the auto-oscillation frequency, the threshold current (I_{th}) for auto-oscillation strongly depends on the constriction width. In fact, it has been observed that the threshold current density increases with reduction in both K_u and constriction width. From the macrospin model, I_{th} can be written as [37]

$$I_{\text{th}} = \frac{\gamma\alpha}{2|\tau_{\text{DL}}|(\hat{m}_o.\hat{\sigma})}\left(\mu_o M_s + 2B_{\text{int}} - \frac{B_{\text{int}}^2}{2M_s}\right). \tag{8}$$

Here, $|\tau_{\text{DL}}|$ is the magnitude of dampinglike SOT; $(\hat{m}_o\hat{\sigma})$ is the cosine of the angle between relaxed magnetization

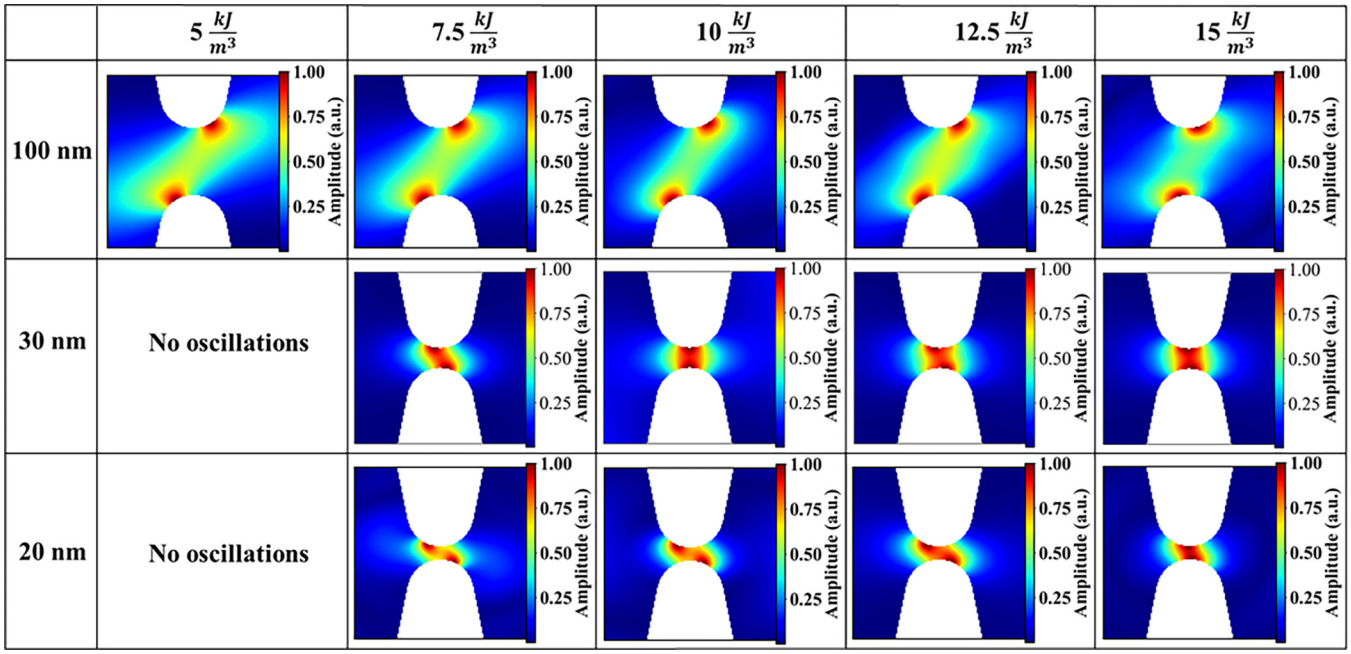

FIG. 4. Spatial profile of auto-oscillations at threshold current density for different constriction widths and K_u values.

and spin polarization. Figure 2(c) shows a sharp increase in I_{th} with decreasing K_u for 20-nm constriction as the change in $\boldsymbol{B}_{\text{int}}$ is very steep for narrower constrictions. The auto-oscillation could not be excited for $K_u = 5$ kJ/m^3 even at current densities of approximately 7 TA/m^2 for both 20- and 30-nm constrictions. This limitation arises from the substantial $\boldsymbol{B}_{\text{demag}}$ at the constriction region, which impedes the excitation of auto-oscillation as the SOT fails to compensate τ_D. Additionally, the nonuniform distribution of current density at the constriction leads to a strongly nonuniform spin current injection and SOT magnitude in the FM layer. Hence, the spatial distribution of auto-oscillation amplitude varies significantly with the constriction width. This variation leads to a pronounced disparity in dynamic $\boldsymbol{B}_{\text{int}}$ across different constriction widths. This results in a variation of threshold current density for different constriction widths, which is not observed in SHNOs biased with an external magnetic field [29].

Figure 4 displays the spatial profiles of auto-oscillation amplitude at the threshold current density. These profiles are observed at a central region of the geometry, which has dimensions of 2×2 μm^2. These spatial profiles are obtained by performing FFT on the spatiotemporal data corresponding to the oscillation in each cell. Notably, the localization of auto-oscillation amplitude varies across different constriction widths. This variation is because the formation of SW wells at the constrictions is governed by the spatial profile of $\boldsymbol{B}_{\text{int}}$ (shown in Appendix F). Total internal effective magnetic field $\boldsymbol{B}_{\text{int}}$ has a local minimum near the edges of the constriction. These SW wells are the points where the amplitude of the auto-oscillation is maximum. In the case of 100-nm constriction, as the current increases, SW modes emerge at opposite edges of the constriction. However, with an increase in uniaxial anisotropy constant (K_u), these modes gradually move towards each other (Fig. 4) and try to align with the easy axis with increase in K_u. Beyond a critical current, these modes detach from the edges and begin propagating. The alignment of edge modes at the opposite constriction edges in narrow constrictions differs from that of 100-nm constrictions due to the proximity of the constriction edges. This proximity leads to the dominance of the demagnetization field over other fields, resulting in a negative sign for the y component of $\boldsymbol{B}_{\text{int}}$. The opposite direction of the $\boldsymbol{B}_{\text{int}}$ at different constrictions leads to alignment of spin-wave wells exhibiting positive and negative slopes from the x axis, corresponding to wider and narrower constrictions, respectively. Additionally, in 20- and 30-nm constrictions, the SW wells occupy the entire available volume within the constriction.

The nonuniformity in the spatial profile of auto-oscillation amplitude can be experimentally detected through optical probing of the constriction region [16]. However, electrical detection of auto-oscillation in SHNO device is more important particularly for practical applications. Therefore, we investigate how the constriction width influences the spatial average of auto-oscillation amplitude in the constriction region. An increase in the peak amplitude of the auto-oscillation with uniaxial anisotropy and current for all the constriction widths is observed (Fig. 5). Higher amplitude at higher current densities results from increased SOT at the constriction, dragging the magnetization away from easy axis towards the spin-polarization direction. Analyzing the $\boldsymbol{B}_{\text{int}}$ distribution at the constriction for three different constriction widths we find that the changes in $\boldsymbol{B}_{\text{int}}$ at similar current densities are a consequence of the competition between $\boldsymbol{B}_{\text{anis}}$ and $\boldsymbol{B}_{\text{demag}}$. As both fields are opposite to each other, high $\boldsymbol{B}_{\text{anis}}$ results in higher value of $\boldsymbol{B}_{\text{int}}$. Closer proximity of spin-wave wells at higher $\boldsymbol{B}_{\text{int}}$ leads to a larger auto-oscillation area, hence increasing the total auto-oscillation amplitude. In contrast, a decrease in auto-oscillation amplitude with constriction width is attributed to the dominating $\boldsymbol{B}_{\text{demag}}$. High $|\boldsymbol{B}_{\text{int}}|$ gives rise

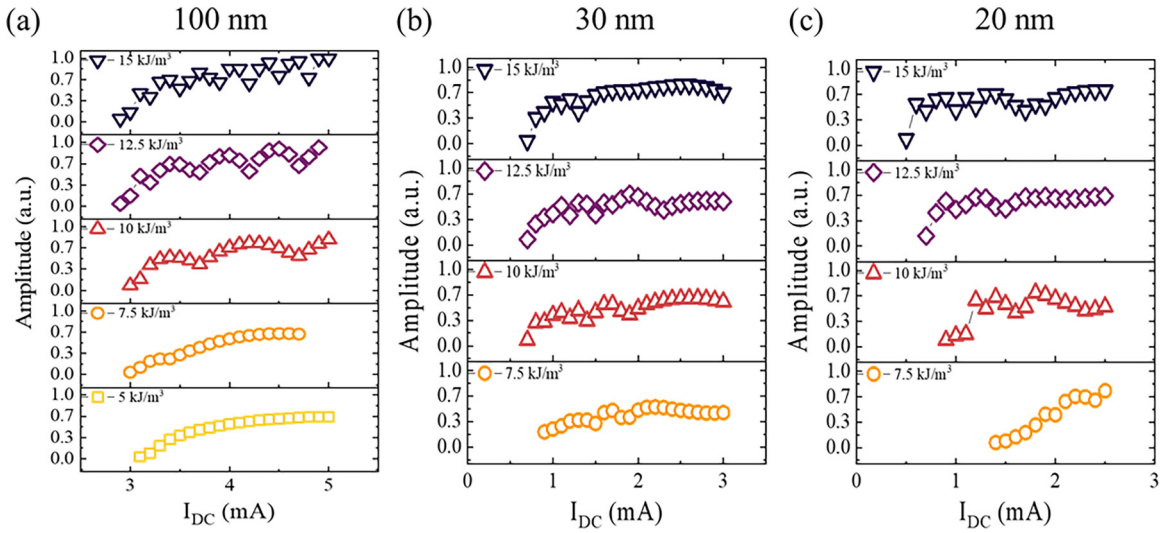

FIG. 5. Variation of amplitude of auto-oscillations with input current for different constriction sizes at different K_u values. (a) 100 nm, (b) 30 nm, and (c) 20 nm.

to strong damping torque, which reduces the auto-oscillation amplitude.

IV. CONCLUSION

To conclude, our study demonstrates significant variations in the auto-oscillation properties of uniaxial anisotropy-assisted external field free spin Hall nano-oscillators (SHNOs) in correlation with different constriction widths. The magnetization dynamics in wide constrictions is primarily influenced by the anisotropy field, resulting in a monotonous frequency redshift with increasing input dc current. In contrast, the magnetization dynamics in narrow constriction is predominantly governed by dipolar interactions, leading to a frequency blueshift. Moreover, we have observed distinctive width-dependent behavior of the SW modes forming within the constrictions. In 100-nm-wide constriction, the SW wells are localized at the opposite edges of the constriction, whereas for the narrow constrictions the SW wells are more centralized within the constriction exhibiting opposite orientation with respect to the wider constrictions due to the dominant effect of $\boldsymbol{B}_{\text{demag}}$. For wider constrictions, the SW modes stick to the edges of the constriction, whereas for narrower (20 and 30 nm) constrictions these modes are inherently different and predominantly occupy the entire constriction region from the auto-oscillation threshold. In addition, the orientations of the SW modes with respect to the constriction width are opposite for wider (100 nm) and narrower (20 and 30 nm) constrictions. Furthermore, our results show that the miniaturization of field free SHNOs essentially leads to lower threshold current of auto oscillation. However, wider constriction provides higher oscillation amplitude and better frequency tunability with input current. These findings illuminate the field free auto-oscillation dynamics of SHNOs across varying constriction length scales, opening avenues for their application in diverse unconventional computing schemes like neuromorphic computing, reservoir computing, and probabilistic computing.

The data that support the findings of this study are available from the corresponding author upon reasonable request.

ACKNOWLEDGMENTS

A.K.G. acknowledges IIT Kanpur for providing financial support through institute fellowship. R.M. acknowledges Initiation Grant, IIT Kanpur, and I-HUB Quantum Technology Foundation, IISER Pune for financial support. S.M. acknowledges the NTU-Research Scholarship (NTU-RSS). R.S.R. acknowledges the support from (i) the Ministry of Education, Singapore under its Academic Research Tier 1 Grants No. 2020-T1-002-084 (Grant No. RP 2/20 RSR) and No. RG76/22 (No. RP 6/22 RSR), and (ii) National Research Foundation Grant No. NRF-CRP21-2018-0003. A.K.G. and R.M. acknowledges the PARAM Sanganak facility at IIT Kanpur.

APPENDIX A: B_{int} FOR DIFFERENT CONSTRICTION WIDTHS AT DIFFERENT K_u VALUES

Figure 6 displays $\boldsymbol{B}_{\text{int}}$ for various constriction widths and K_u values. In the case of the 100 nm width, $\boldsymbol{B}_{\text{anis}}$ dominates, leading to an increase in $\boldsymbol{B}_{\text{int}}$ with higher K_u. Additionally, at larger K_u values, $\boldsymbol{B}_{\text{int}}$ steeply decreases due to the increased auto-oscillation amplitude. For narrower constrictions, $\boldsymbol{B}_{\text{int}}$ becomes negative as a result of the heightened influence of $\boldsymbol{B}_{\text{demag}}$. At higher K_u values, $\boldsymbol{B}_{\text{int}}$ becomes less negative for narrower constrictions and exhibits a higher positive value for wider constriction, primarily due to the increasing contribution from $\boldsymbol{B}_{\text{anis}}$.

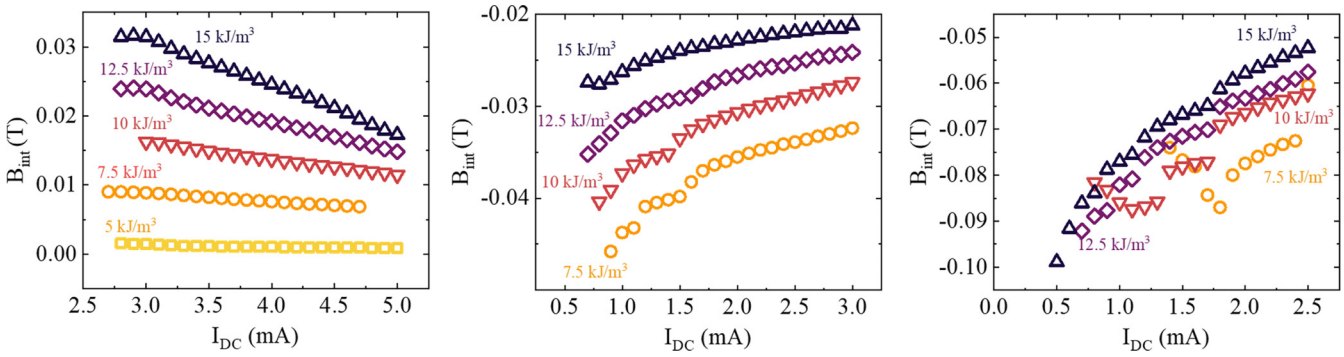

FIG. 6. B_{int} at constriction widths at different K_u as a function of current have been plotted: (a) 100 nm, (b) 30 nm, and (c) 20 nm.

APPENDIX B: LINEWIDTH VARIATION OF AUTO-OSCILLATIONS WITH CONSTRICTION WIDTH, INPUT CURRENT, AND K_u

Figure 7 displays the linewidth variation of auto oscillations at different constriction widths. For the 100-nm constriction, the fluctuations in Δf increase as K_u is raised. The oscillation amplitude undergoes harmonic splitting due to high $\boldsymbol{B}_{\text{int}}$ at higher K_u values, resulting in broadened peaks. In contrast, for the 20- and 30-nm constrictions, Δf fluctuations occur at lower I_{dc} values but diminish as $\boldsymbol{B}_{\text{int}}$ stabilizes. Lower constrictions exhibit improved linewidth, potentially attributable to the proximity of edge modes within the constriction [38,39].

APPENDIX C: ANGULAR VARIATION OF AUTO-OSCILLATION AMPLITUDE FOR DIFFERENT CONSTRICTION WIDTHS

Auto-oscillation amplitude for different constriction widths at different in-plane angles of the uniaxial anisotropy is shown in Fig. 8. 100 nm has peak amplitude around 75° and the width of the peak is larger than the other constriction widths. Other two narrow constrictions have the peak amplitude at 90°. Still due to the extremely dominant demagnetizing effects at 20-nm NC width the amplitude at 85° is considerably lower than that of the 30 nm.

APPENDIX D: COEFFICIENT OF NONLINEAR FREQUENCY SHIFT AT $K_u = 15\ \text{kJ/m}^3$

Coefficient of nonlinear frequency shift [as given in Eq. (6)] is plotted against I_{dc} for 100-nm constriction width at $K_u = 15\ \text{kJ/m}^3$. As explained in the main text the shift in frequency from the simulation results approximately matches with the theoretical prediction, where N stays negative for 100 nm and positive for the narrow constrictions.

In Eq. (7), Slavin *et al.* [14] assumed an infinite thin film in the y-z plane with constant demagnetizing effect along its thickness to get Eq. (6). The applied field is taken to be in plane along the z direction with a constant magnitude. Resulting excitation is thought of as a standing self-localized wave bullet which is confined in the constriction. Field, and in turn

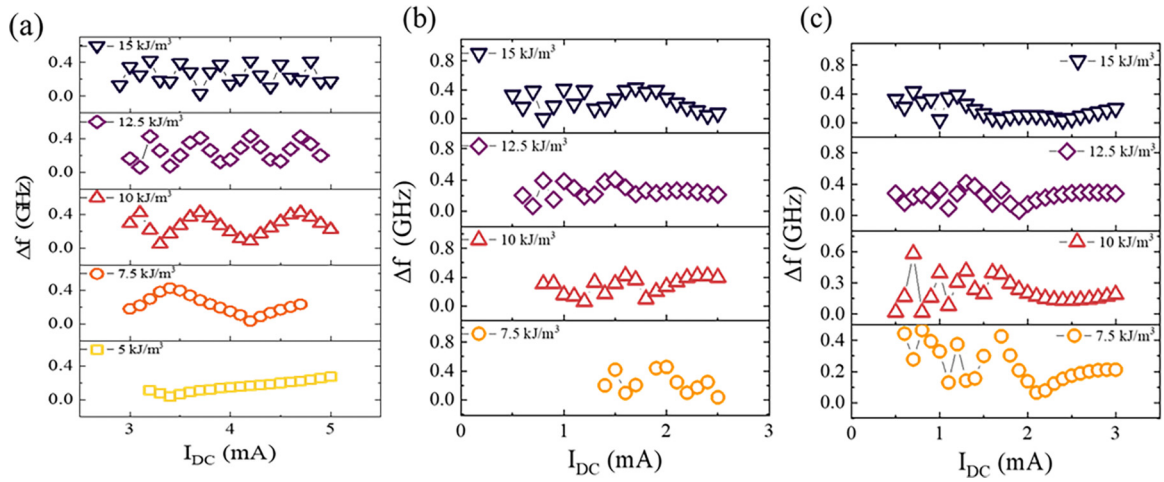

FIG. 7. Linewidth of auto-oscillations at different K_u as a function of current have been plotted: (a) 100 nm, (b) 20 nm, and (c) 30 nm.

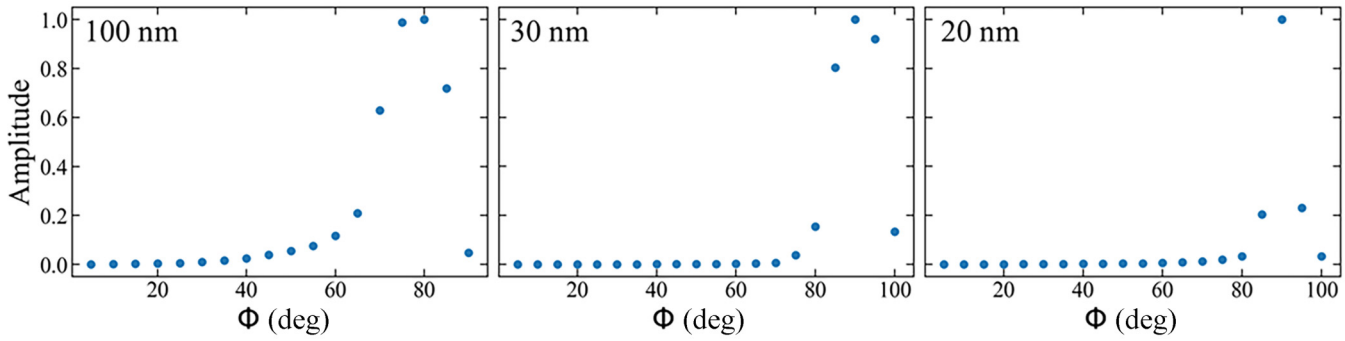

FIG. 8. FFT amplitude of auto-oscillations as a function of angle of effective field for different constriction widths.

the nonlinearity coefficient, is assumed to be constant as the current is fixed, which differs from our results where both of them are a function of I_{dc}. Power of auto-oscillations P is also a function of current as amplitude depends on I_{dc}.

$$\omega = \omega_o + NP,$$

$$\frac{\delta\omega}{\delta I} = N\frac{\delta \mathrm{P}}{\delta \mathrm{I}} + \frac{\delta N}{\delta I}P.$$

Also, the frequency of spin-wave bullet is single modal while in our case the field free auto-oscillation has multiple modes. Thus, only a qualitative comparison between the simulation and analytical results is made.

Figure 9 shows the total shift in the frequency of the oscillations with the current in the arbitrary units. For the 100-nm constriction the shift is negative with decrement in the value with increase in I_{dc}. See Fig. 10.

APPENDIX E: AUTO-OSCILLATION SPECTRA FOR DIFFERENT CONSTRICTION WIDTHS AS A FUNCTION OF CURRENT

Frequency response at 6 different constriction widths (100 nm – 20 nm) is shown in Fig. 11. The dynamics until 40-nm constriction width is similar to that of 100 nm, while at 20- and 30-nm constriction width the magnetodynamical behavior is different. Again it is because until 40-nm constriction width the $\boldsymbol{B}_{\mathrm{anis}}$ contribution to the $\boldsymbol{B}_{\mathrm{int}}$ is greater than that of $\boldsymbol{B}_{\mathrm{demag}}$ which makes the $\boldsymbol{B}_{\mathrm{int}}$ positive. Consequently, the nonlinear frequency shift is negative until 40-nm constriction width. Below the 40-nm constriction width the contribution of $\boldsymbol{B}_{\mathrm{demag}}$ towards $\boldsymbol{B}_{\mathrm{int}}$ dominates and the magnetodynamic nonlinearity changes sign. The frequency response with current $\frac{\delta f}{\delta I}$ is positive for narrower constrictions.

APPENDIX F: SPATIAL PROFILE OF B_{int} AND SPECTRAL DISTRIBUTION OBTAINED FROM FFT

It can be seen from Fig. 12 that the spatial profile of the auto-oscillation follows the distribution of the $\boldsymbol{B}_{\mathrm{int}}$. Constricted edges at the nanoconstriction produce a very strong demagnetizing effect due to robust dipolar interactions. The direction of the $\boldsymbol{B}_{\mathrm{demag}}$ due to these effects is opposite to the $\boldsymbol{B}_{\mathrm{anis}}$. As evident frm the Fig. 1 in the main text, the direction of $\boldsymbol{B}_{\mathrm{Oe}}$ is also opposite to the $\boldsymbol{B}_{\mathrm{anis}}$ at the NC. Contributions from the $\boldsymbol{B}_{\mathrm{demag}}$ and $\boldsymbol{B}_{\mathrm{anis}}$ leads overall reduction in total internal field at the constriction. At some points near the

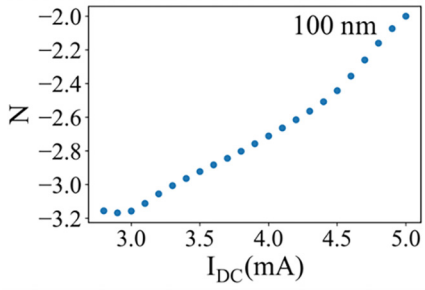

FIG. 9. Nonlinear frequency shift for different constriction widths at $K_u = 15$ kJ/m^3.

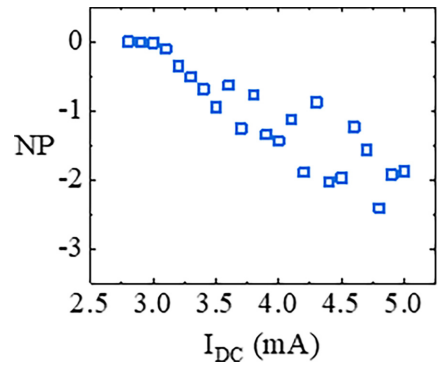

FIG. 10. Nonlinear frequency shift × power for 100-nm constriction width at $K_u = 15$ kJ/m^3 as a function of input current.

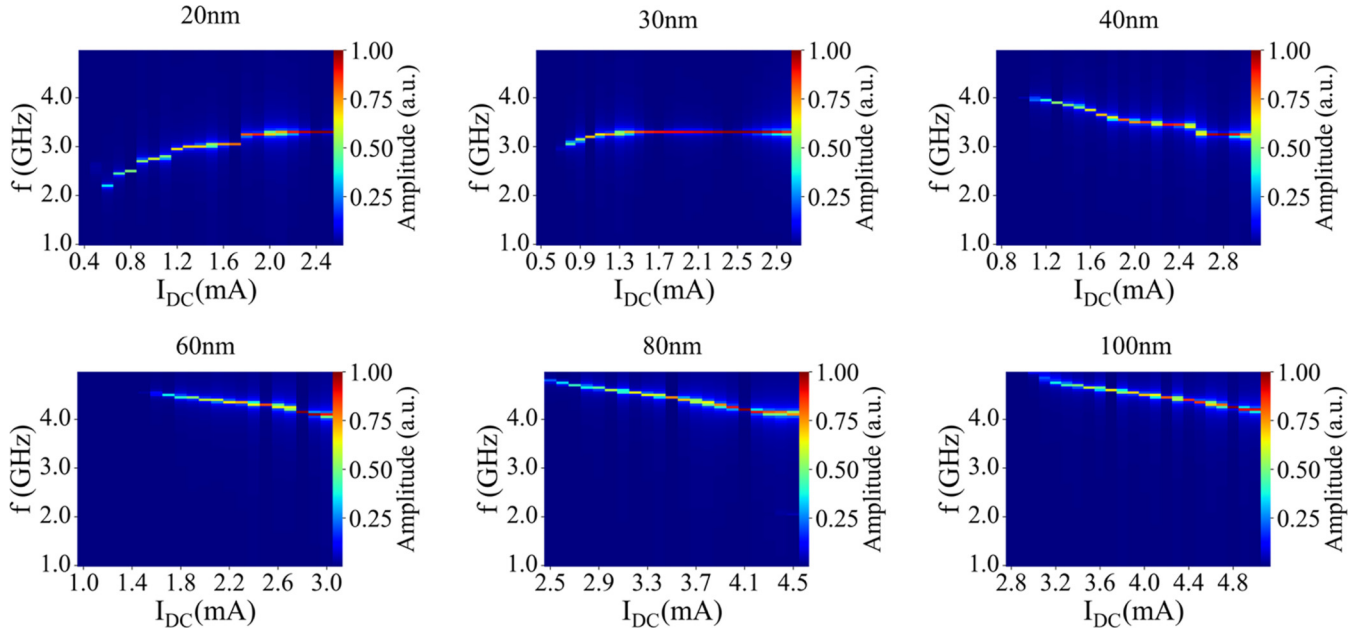

FIG. 11. Auto-oscillation power spectral densities (PSDs) at $K_u = 15\text{kJ/m}^3$ from constriction widths from 20 to 100 nm as a function of current are plotted. Color bars represent the auto-oscillation amplitude in arbitrary units.

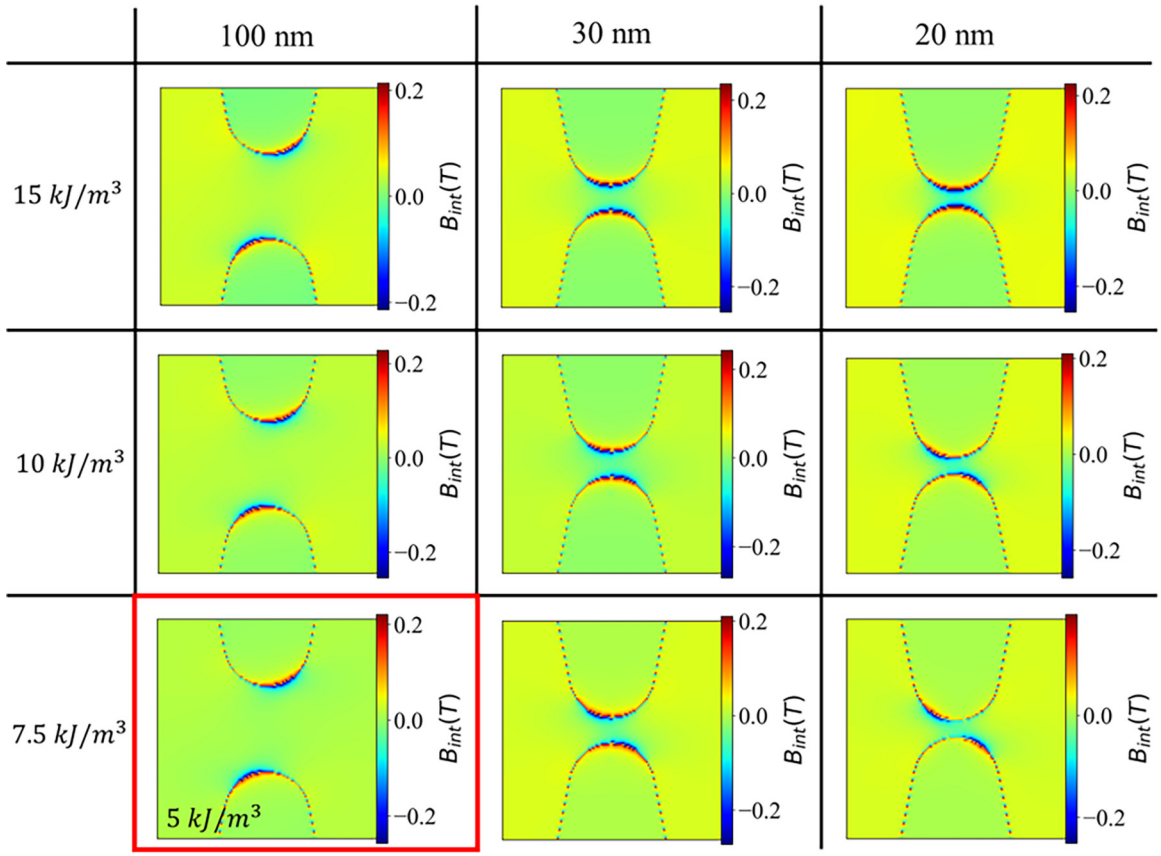

FIG. 12. $\boldsymbol{B}_{\text{int}}$ distribution at the I_{th} for different constriction sizes. The bottommost plot for 100-nm constriction (marked by a red outline) refers to the $K_u = 5\ \text{kJ/m}^3$.

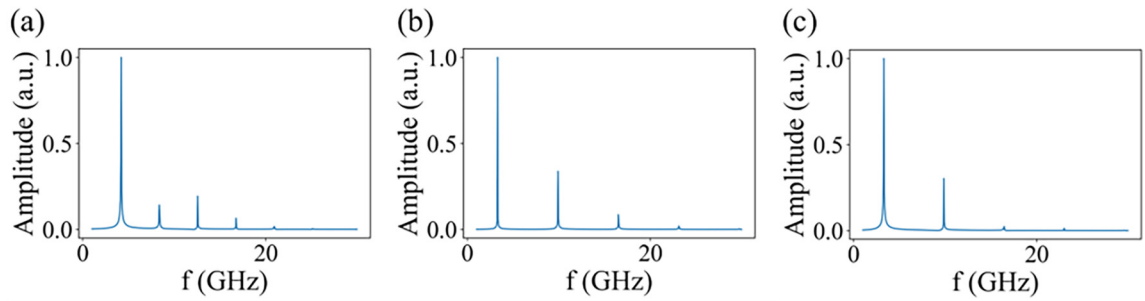

FIG. 13. FFT spectra of oscillation at $K_u = 15$ kJ/m^3 for (a) 100 nm, (b) 30 nm, and (c) 20 nm at their maximum drive current.

edges of the constriction the $\boldsymbol{B}_{\text{demag}}$ is significantly lower than the rest of the constriction. Total internal effective magnetic field has a local minimum, i.e., SW wells at these points near the edges of the constriction. These SW wells form a localized oscillation mode which is nonpropagating, and are the points where the amplitude of the auto-oscillation is maximum.

The output signal from the SHNO is made up of multiple frequencies. These frequencies can be extracted by doing a FFT of the obtained the dynamics. As can be seen from Fig. 13 the FFT amplitude of these additional modes is comparably minute to the amplitude of the first harmonic.

APPENDIX G: THE TRAJECTORY OF $\vec{M}$ AT THE POINT OF FREQUENCY DROP FOR 20-NM CONSTRICTION

Figure 14 shows the magnetization vector's 3d trajectories at the point of frequency drop. It is observed that around the frequency drop the trajectory of $\boldsymbol{M}$ becomes bigger, which results in high amplitude of precession.

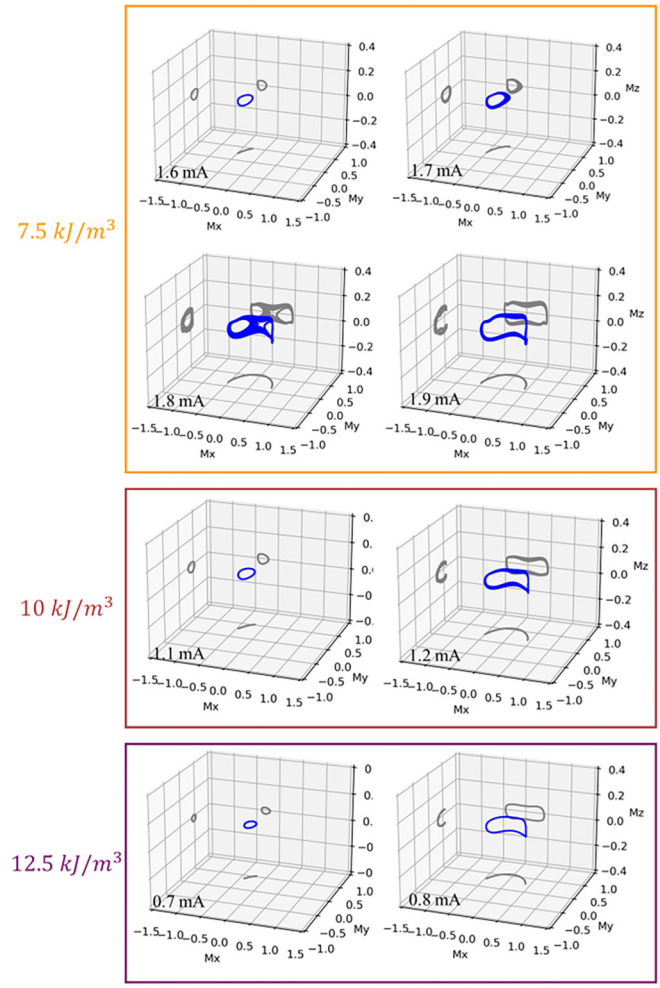

FIG. 14. The 3D trajectory of auto-oscillations at 20-nm constriction around the point of frequency drop.

[1] J. Puebla, J. Kim, K. Kondou, and Y. Otani, Spintronic devices for energy-efficient data storage and energy harvesting, Commun. Mater. **1**, 1 (2020).

[2] P. Dürrenfeld, A. A. Awad, A. Houshang, R. K. Dumas, and J. Åkerman, A 20 nm spin Hall nano-oscillator, Nanoscale **9**, 1285 (2017).

[3] A. Kumar, H. Fulara, R. Khymyn, A. Litvinenko, M. Zahedinejad, M. Rajabali, X. Zhao, and J. Åkerman, Robust mutual synchronization in long spin Hall nano-oscillator chains, Nano Lett. **23**, 6720 (2023).

[4] R. Sharma, R. Mishra, T. Ngo, Y.-X. Guo, S. Fukami, H. Sato, H. Ohno, and H. Yang, Electrically connected spin-torque oscillators array for 2.4 GHz WiFi band transmission and energy harvesting, Nat. Commun. **12**, 1 (2021).

[5] B. Jiang, W. Zhang, H. Zhon, Y. Zhanga, S. Yu, G. Han, S. Xiao, G. Liu, S. Yan, J. Li, and S. Kang, Towards terahertz

spin Hall nano-oscillator with synthesized antiferromagnets, J. Magn. Magn. Mater. **490**, 165470 (2019).

[6] V. E. Demidov, H. Ulrichs, S. V. Gurevich, S. O. Demokritov, V. S. Tiberkevich, A. N. Slavin, A. Zholud, and S. Urazhdin, Synchronization of spin Hall nano-oscillators to external microwave signals, Nat. Commun. **5**, 1 (2014).

[7] B. Jiang, W.-J. Zhang, M. K. Alam, S.-Y. Yu, G.-B. Han, G.-L. Liu, S.-S. Yan, and S.-S. Kang, Synchronization of nanowire-based spin Hall nano-oscillators, Chin. Phys. B **31**, 077503 (2022).

[8] M. Zahedinejad, A. A. Awad, S. Muralidhar, R. Khymyn, H. Fulara, H. Mazraati, M. Dvornik, and J. Åkerman, Two-dimensional mutually synchronized spin Hall nano-oscillator arrays for neuromorphic computing, Nat. Nanotechnol. **15**, 47 (2020).

[9] M. Zahedinejad, H. Fulara, R. Khymyn, A. Houshang, M. Dvornik, S. Fukami, S. Kanai, H. Ohno, and J. Åkerman, Memristive control of mutual spin Hall nano-oscillator synchronization for neuromorphic computing, Nat. Mater. **21**, 81 (2022).

[10] T. Kendziorczyk and T. Kuhn, Mutual synchronization of nanoconstriction-based spin Hall nano-oscillators through evanescent and propagating spin waves, Phys. Rev. B **93**, 134413 (2016).

[11] M. Romera *et al.*, Vowel recognition with four coupled spin-torque nano-oscillators, Nature (London) **563**, 230 (2018).

[12] D. Marković, M. W. Daniels, P. Sethi, A. D. Kent, M. D. Stiles, and J. Grollier, Easy-plane spin Hall nano-oscillators as spiking neurons for neuromorphic computing, Phys. Rev. B **105**, 014411 (2022).

[13] H. Fulara, M. Zahedinejad, R. Khymyn, M. Dvornik, S. Fukami, S. Kanai, H. Ohno, and J. Åkerman, Giant voltage-controlled modulation of spin Hall nano-oscillator damping, Nat. Commun. **11**, 4006 (2020).

[14] A. Kumar, M. Rajabali, V. Hugo González, M. Zahedinejad, A. Houshang, and J. Åkerman, Fabrication of voltage-gated spin Hall nano-oscillators, Nanoscale **14**, 1432 (2022).

[15] L. Chen, Y. Chen, Z. Gao, K. Zhou, Z. Tao, Y. Pu, T. Zhou, and R. Liu, Excitation and voltage-gated modulation of single-mode dynamics in a planar nanogap spin Hall nano-oscillator, Phys. Rev. B **108**, 054425 (2023).

[16] H. Fulara, M. Zahedinejad, R. Khymyn, A. A. Awad, S. Muralidhar, M. Dvornik, and J. Åkerman, Spin-orbit torque–driven propagating spin waves, Sci. Adv. **5**, eaax8467 (2019).

[17] L. Chen, K. Zhou, Z. Tao, Z. Gao, L. Liang, Z. Li, and R. Liu, Self-oscillations in a nanogap spin Hall nano-oscillator with a perpendicularly magnetized external film, Phys. Rev. Appl. **19**, 054051 (2023).

[18] M. Succar and M. Haidar, Spin wave excitations in a nanowire spin Hall oscillator with perpendicular magnetic anisotropy, J. Appl. Phys. **133**, 093901 (2023).

[19] M. Dvornik, A. A. Awad, and J. Åkerman, Origin of magnetization auto-oscillations in constriction-based spin Hall nano-oscillators, Phys. Rev. Appl. **9**, 014017 (2018).

[20] S. M. Mohseni *et al.*, Spin torque-generated magnetic droplet solitons, Science **339**, 1295 (2013).

[21] A. Slavin and V. Tiberkevich, Spin wave mode excited by spin-polarized current in a magnetic nanocontact is a standing self-localized wave bullet, Phys. Rev. Lett. **95**, 237201 (2005).

[22] L. Chen, S. Urazhdin, Y. W. Du, and R. H. Liu, Dynamical mode coupling and coherence in a spin Hall nano-oscillator with perpendicular magnetic anisotropy, Phys. Rev. Appl. **11**, 064038 (2019).

[23] R. H. Liu, W. L. Lim, and S. Urazhdin, Dynamical skyrmion state in a spin current nano-oscillator with perpendicular magnetic anisotropy, Phys. Rev. Lett. **114**, 137201 (2015).

[24] V. E. Demidov, S. Urazhdin, A. Anane, V. Cros, and S. O. Demokritov, Spin–orbit-torque magnonics, J. Appl. Phys. **127**, 170901 (2020).

[25] J. Han, P. Zhang, J. T. Hou, S. A. Siddiqui, and L. Liu, Mutual control of coherent spin waves and magnetic domain walls in a magnonic device, Science **366**, 1121 (2019).

[26] J. E. Hirsch, Spin Hall effect, Phys. Rev. Lett. **83**, 1834 (1999).

[27] S. Y. Huang, D. Qu, T. C. Chuang, C. C. Chiang, W. Lin, and C. L. Chien, Pure spin current phenomena, Appl. Phys. Lett. **117**, 190501 (2020).

[28] J. C. Slonczewski, Current-driven excitation of magnetic multilayers, J. Magn. Magn. Mater. **159**, L1 (1996).

[29] A. A. Awad, A. Houshang, M. Zahedinejad, R. Khymyn, and J. Åkerman, Width dependent auto-oscillating properties of constriction based spin Hall nano-oscillators, Appl. Phys. Lett. **116**, 232401 (2020).

[30] S. Manna, R. Medwal, S. Gupta, J. R. Mohan, Y. Fukuma, and R. S. Rawat, Anisotropy-assisted bias-free spin Hall nano-oscillator, Appl. Phys. Lett. **122**, 072401 (2023).

[31] K. Yogendra, M. Koo, and K. Roy, in *IEEE/ACM International Symposium on Nanoscale Architectures (NANOARCH), Newport, RI, USA* (IEEE, 2017), pp. 89–94.

[32] T. Shirokura and P. N. Hai, Bias-field-free spin Hall nano-oscillators with an out-of-plane precession mode, J. Appl. Phys. **127**, 103904 (2020).

[33] P. M. Haney, H.-W. Lee, K.-J. Lee, A. Manchon, and M. D. Stiles, Current induced torques and interfacial spin-orbit coupling: Semiclassical modeling, Phys. Rev. B **87**, 174411 (2013).

[34] T. Nan, S. Emori, C. T. Boone, X. Wang, T. M. Oxholm, J. G. Jones, B. M. Howe, G. J. Brown, and N. X. Sun, Comparison of spin-orbit torques and spin pumping across NiFe/Pt and NiFe/Cu/Pt interfaces, Phys. Rev. B **91**, 214416 (2015).

[35] D. C. Ralph and M. D. Stiles, Spin transfer torques, J. Magn. Magn. Mater. **320**, 1190 (2008).

[36] Z. Gao, Y. Chen, L. Chen, G. Zhu, Z. Li, and R. Liu, Dynamical modes in a vertical nanocontact-based spin Hall nano-oscillator, Phys. Rev. B **107**, 214410 (2023).

[37] A. N. Slavini and P. Kabos, Approximate theory of microwave generation in a current-driven magnetic nanocontact magnetized in an arbitrary direction, IEEE Trans. Magn. **41**, 1264 (2005).

[38] B. Divinskiy, S. Urazhdin, S. O. Demokritov, and V. E. Demidov, Controlled nonlinear magnetic damping in spin-Hall nano-devices, Nat. Commun. **10**, 1 (2019).

[39] I. Lee, C. Zhang, S. Singh, B. McCullian, and P. C. Hammel, Origin of nonlinear damping due to mode coupling in auto-oscillatory modes strongly driven by spin-orbit torque, Phys. Rev. Appl. **17**, 064047 (2022).